

PAPER

Effective locomotion at multiple stride frequencies using proprioceptive feedback on a legged microrobot

To cite this article: Neel Doshi *et al* 2019 *Bioinspir. Biomim.* **14** 056001

View the [article online](#) for updates and enhancements.

Recent citations

- [Kaushik Jayaram *et al*](#)
- [Wei Gao *et al*](#)
- [Viscoelastic legs for open-loop control of gram-scale robots](#)
Ryan St Pierre *et al*



IOP | ebooks™

Bringing together innovative digital publishing with leading authors from the global scientific community.

Start exploring the collection—download the first chapter of every title for free.

Bioinspiration & Biomimetics



PAPER

Effective locomotion at multiple stride frequencies using proprioceptive feedback on a legged microrobot

RECEIVED
24 January 2019

REVISED
2 June 2019

ACCEPTED FOR PUBLICATION
12 June 2019

PUBLISHED
1 July 2019

Neel Doshi^{1,2,3} , Kaushik Jayaram^{1,2,3} , Samantha Castellanos^{1,2}, Scott Kuindersma¹ and Robert J Wood^{1,2}

¹ John A. Paulson School of Engineering and Applied Sciences, Harvard University, Cambridge, MA, United States of America

² Wyss Institute for Biologically Inspired Engineering, Cambridge, MA, United States of America

³ These authors contributed equally.

E-mail: ndoshi@seas.harvard.edu and kjayaram@seas.harvard.edu

Keywords: self-sensing, legged microrobots, piezoelectric actuation, robust locomotion, linear-quadratic-Gaussian control

Supplementary material for this article is available [online](#)

Abstract

Limitations in actuation, sensing, and computation have forced small legged robots to rely on carefully tuned, mechanically mediated leg trajectories for effective locomotion. Recent advances in manufacturing, however, have enabled in such robots the ability for operation at multiple stride frequencies using multi-degree-of-freedom leg trajectories. Proprioceptive sensing and control is key to extending the capabilities of these robots to a broad range of operating conditions. In this work, we use concomitant sensing for piezoelectric actuation with a computationally efficient framework for estimation and control of leg trajectories on a quadrupedal microrobot. We demonstrate accurate position estimation ($<16\%$ root-mean-square error) and control ($<16\%$ root-mean-square tracking error) during locomotion across a wide range of stride frequencies (10 Hz–50 Hz). This capability enables the exploration of two bioinspired parametric leg trajectories designed to reduce leg slip and increase locomotion performance (e.g. speed, cost-of-transport (COT), etc). Using this approach, we demonstrate high performance locomotion at stride frequencies (10 Hz–30 Hz) where the robot's natural dynamics result in poor open-loop locomotion. Furthermore, we validate the biological hypotheses that inspired the trajectories and identify regions of highly dynamic locomotion, low COT (3.33), and minimal leg slippage ($<10\%$).

1. Introduction

Terrestrial animals use a variety of complex leg trajectories to navigate natural terrains [1]. The choice of leg trajectory is often determined by a combination of morphological factors including posture [2], hip and leg kinematics [3], ankle and foot designs [4], and actuation capabilities (e.g. muscle mechanics [5, 6]). In addition, animals also modify their leg trajectories to meet performance requirements such as speed [7], stability [8, 9], and economy [10], as well as to adapt to external factors such as terrain type [11, 12] and surface properties [13, 14].

Inspired by their biological counterparts, large (body length (BL) ~ 100 cm) bipedal [15, 16] and quadrupedal [17–20] robots typically have two or more actuated degrees-of-freedom (DOF) per leg to enable complex leg trajectories. This dexterity is leveraged in a variety of control schemes to adapt to

different environments and performance requirements. For example, optimization algorithms have been used to command leg trajectories to enable stable, dynamic locomotion on the Atlas bipedal [21] and HyQ quadrupedal [19] robots. Furthermore, the MIT Cheetah [18] relies on a hierarchical control scheme where the low-level controllers alter leg trajectories to directly modulate ground reaction forces.

However, as the robot's size decreases, manufacturing and material limitations constrain the number of actuators and sensors. Consequently, a majority of medium (BL ~ 10 cm) [22] and small (BL ~ 1 cm) [23–25] legged robots have at most single DOF legs driven by a hip actuator. In such systems, leg trajectory is dictated by the transmission design, and these robots often rely on tuned passive dynamics to achieve efficient locomotion [26, 27]. Nevertheless, careful mechanical design allows these robots to demonstrate impressive capabilities, including high-speed running

[28], jumping [29], climbing [30, 31], horizontal to vertical transitions [12], and confined space locomotion [14].

Recent work has also focused on developing whole-body locomotion control schemes for the autonomous operation of these small legged robots. These include controllers designed using stochastic kinematic models on the octopedal OctoRoACH [32] and using deep reinforcement learning on the hexapedal VelociRoACH [33] robots. However, these robots do not have the mechanical dexterity to actively vary the shape of their leg trajectory and instead rely on mechanical tuning and inter-leg timing (i.e. gait) to achieve effective locomotion at a specific operating frequency. In contrast, the Harvard Ambulatory MicroRobot (HAMR, figure 1(a)) is able to independently control the fore-aft and vertical position of each leg using high-bandwidth piezoelectric bending actuators. This dexterity enables control over both the shape of individual leg trajectories and gait. Furthermore, HAMR is unique among legged robots in its ability to operate at a wide range of stride frequencies. Despite this dexterity, however, a lack of sensing and control has limited its operation to using feed-forward sinusoidal voltage inputs resulting in elliptical leg trajectories [34, 35]. Though this approach has previously enabled rapid locomotion [36], high-performance operation (e.g. high speed, low COT, etc) has been limited to a narrow range of stride frequencies [37].

In this work, we leverage concomitant sensing for piezoelectric actuation (figure 1(b), [38]) and a computationally inexpensive estimator and controller (figure 1(c)) for tracking leg trajectories on a microrobot. The robot and concomitant sensors and discussed in section 2. We then describe the estimator (section 3) and controller (section 4) and include an important simplification, treating of ground contact as a perturbation. We leverage this capability to track two bioinspired parametric leg trajectories that modulate intra-leg timing, energy, and stiffness (section 5). We experimentally evaluate these trajectories (section 6), and demonstrate that our framework enables accurate estimation (section 7.1) and tracking (section 7.2) for our operating conditions (10 Hz–50 Hz). Furthermore, we find that these trajectories allow the robot to maintain locomotion performance in the body dynamics frequency regime by reducing leg slip, improving COT, and favorably utilizing body dynamics (section 8). We generalize these results across the range of operating stride frequencies in section 9, and discuss implications of this work and potential future extensions in section 10.

2. Platform overview

This section describes the relevant properties of the microrobot (section 2.1) and the concomitant sensors (section 2.2).

2.1. Robot description

HAMR (figure 1(a)) is a 4.5 cm long, 1.43 g quadrupedal microrobot with eight independently actuated DOFs [39]. Each leg has two DOFs that are driven by optimal energy density piezoelectric bending actuators [40]. These actuators are controlled with AC voltage signals using a simultaneous drive configuration described by Karpelson *et al* [41]. A spherical-five-bar (SFB) transmission connects the two actuators to a single leg in a nominally decoupled manner: the swing actuator controls the leg's fore-aft position, and the lift actuator controls the leg's vertical position. A minimal-coordinate representation of the pseudo-rigid body dynamics of this robot has a configuration vector $q = [q^{fb}, q^a]^T \in \mathbb{R}^{14}$ and takes the AC voltages signals $u^a \in \mathbb{R}^8$ as inputs. The configuration vector consists of the floating base position and orientation ($q^{fb} \in \mathbb{R}^6$), and the tip deflections of the eight actuators ($q^a \in \mathbb{R}^8$). An alternative minimal-coordinate representation occasionally used in this work is $q^{alt} = [q^{fb}, q^l]^T \in \mathbb{R}^{14}$. Here $q^l \in \mathbb{R}^8$ is the vector of the four legs' fore-aft (F) and vertical (V) positions, and it is related to q^a by a one-to-one kinematic transformation.

2.2. Sensor design and dynamics

Eight off-board piezoelectric encoders provide measurements of actuator tip-velocities ($\dot{q}^a \in \mathbb{R}^8$) [38]. Though these sensors are currently off-board, an on-board implementation is straightforward as the components are both light (<10 mg) and small (<5 mm²). Previous work has shown that the tip-velocity of the i th actuator (\dot{q}_i^a) is α times the *mechanical current* (i^m) produced by that actuator's motion; that is,

$$\dot{q}_i^a = \alpha i^m. \quad (1)$$

Each encoder (figure 1(b)) measures the mechanical current by applying Kirchoff's law to the measurement circuit in series with a lumped-parameter electrical model of an actuator:

$$i^m = \frac{V^m - V}{R_s} - \beta C \dot{V} - \frac{V}{R}. \quad (2)$$

The first term on the RHS of equation (2) is the total current drawn by an actuator computed from measurements of the voltage before (V^m) and after (V) a shunt resistor ($R_s = 75 \text{ k}\Omega$). The actuator is modeled as a capacitor (C), resistor (R), and current source (i^m) in parallel. The voltage and frequency dependent values of R and C have been computed for our operating conditions by Jayaram *et al* [38]. Finally, β is a blocking factor which accounts for imperfect measurements of C , and is set to 1.57 as described by Jayaram *et al* [38].

3. Estimator design

We use the sensors described above in a proprioceptive estimator for leg position and velocity

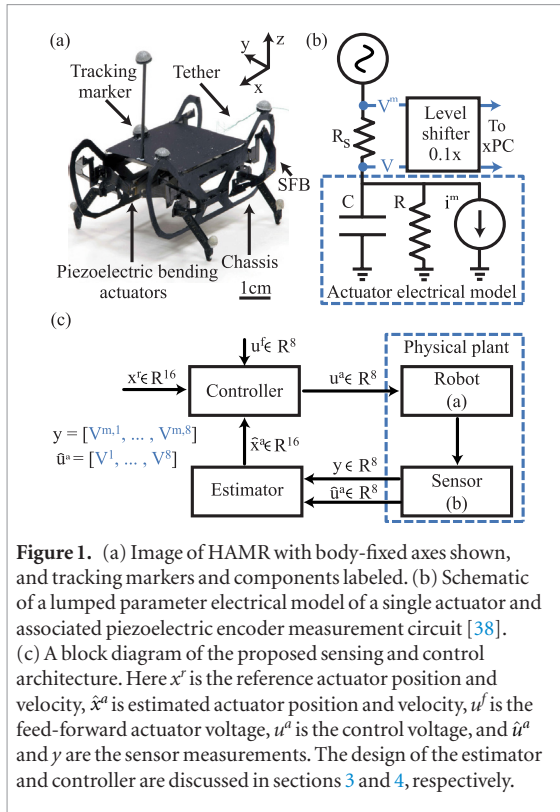


Figure 1. (a) Image of HAMR with body-fixed axes shown, and tracking markers and components labeled. (b) Schematic of a lumped parameter electrical model of a single actuator and associated piezoelectric encoder measurement circuit [38]. (c) A block diagram of the proposed sensing and control architecture. Here x^a is the reference actuator position and velocity, \hat{x}^a is estimated actuator position and velocity, u^a is the feed-forward actuator voltage, u^c is the control voltage, and \hat{u}^a and y are the sensor measurements. The design of the estimator and controller are discussed in sections 3 and 4, respectively.

($x^a = [q^a, \dot{q}^a]^T \in \mathbb{R}^{16}$). These estimates are used with a feedback controller to command a variety of leg trajectories for improved locomotion. Previous work has focused on the estimation of the floating-base position and velocity for legged systems. This includes approaches that use simplified dynamic models [42], kinematic approaches [43], hybrid models [44], sampling-based techniques (e.g. particle filters [45] or unscented Kalman filters [46]), and more recently, high-fidelity process models that resolve the discontinuous mechanics of ground contact online [47].

For our application, size and payload constraints make it difficult to incorporate additional sensors on the microrobot. This combined with strict computational constraints makes it impractical to use many of the aforementioned approaches. As such, we utilize an infinite-horizon Kalman filter that combines a linear approximation of the transmission model in the absence of contact with the measurement model described in equations (1) and (2). To simplify the measurement model, we leverage the one-to-one map between leg and actuator position to work in the actuator frame. Our filter averages a drifting position measurement that registers ground contact with a zero-drift position prediction that ignores contact, with the primary advantage that all quantities used in the update rule are pre-computed.

3.1. Process model

Given that we are ignoring ground contact, a single transmission can be modeled in isolation. The minimal-coordinate dynamics of each SFB transmission in the absence of contact is described by the continuous nonlinear difference equation:

$$x_{k+1}^p = f(x_k^p, u_k^p), \quad (3)$$

where k is the time-step, $x_k^p = [q_k^s, \dot{q}_k^s, q_k^l, \dot{q}_k^l]^T \in \mathbb{R}^4$ is the position and velocity of the swing and lift actuators, and $u_k^p = [V_k^s, V_k^l]^T \in \mathbb{R}^2$ are the actuator drive voltages. A detailed derivation of $f(x_k^p, u_k^p)$ is presented in Note S1. Instead of calculating the linear approximation of $f(x_k^p, u_k^p)$ about a fixed point (x_0^p, u_0^p), we use MATLAB's subspace identification algorithm `n4sid` [48, 49] to determine a discrete-time second-order (four-state) linear system that minimizes the prediction error for the range of expected actuator deflections (± 0.15 mm) and stride frequencies (10 Hz–50 Hz). While the accuracy of a local linear approximation decreases away from the fixed point, the identified model is accurate in an average sense across the range of expected operating conditions. The resulting discrete-time linear system has the form:

$$x_{k+1}^p = A^p x_k^p + B^p (u_k^p - u_0^p) + w_k^p, \quad (4)$$

with $A^p \in \mathbb{R}^{4 \times 4}$ and $B^p \in \mathbb{R}^{4 \times 2}$. Moreover, the signal $w_k^p \in \mathbb{R}^4$ is zero-mean process noise with covariance W^p . The `n4sid` algorithm determines the system matrices (A^p and B^p) and noise covariance (W^p) of the zero-mean process noise that minimize the squared prediction error in $x_k^p - x_0^p$ when driven with voltages $u_k^p - u_0^p$. We describe the identification process in evaluating the accuracy of the resulting model in Note S2. Finally, we note that x^p and u^p are subsets of x^a and u^a corresponding to the appropriate transmission, and the identical procedure is carried out to identify a process model for each transmission.

3.2. Measurement model

Since each piezoelectric encoder measurement is independent, the sensor dynamics (section 2.2) is inverted to form the measurement model for a single actuator. We start by combining equations (1) and (2) with a finite difference approximation of \dot{V} to write a difference equation for \dot{q}_k :

$$\dot{q}_k = c_1(V_k^m - V_k) - c_2 V_k - c_3(V_k - V_{k-1}), \quad (5)$$

where $c_1 = \alpha R_s^{-1}$, $c_2 = \alpha R^{-1}$, and $c_3 = \alpha \beta C h^{-1}$. Since equation (5) depends on the previous time-step, we also write a difference equation for \dot{q}_{k-1} using the same finite difference approximation for \dot{V}_{k-1} :

$$\dot{q}_{k-1} = c_1(V_{k-1}^m - V_{k-1}) - c_2 V_{k-1} - c_3(V_{k-1} - V_{k-2}). \quad (6)$$

Combining equations (5) and (6) and solving for $y_k^m = [V_k^m, V_{k-1}^m] \in \mathbb{R}^2$ gives the measurement model:

$$y_k^m = H^m x_k^m + D^m u_k^m + n_k^m. \quad (7)$$

Here

$$H^m = \frac{1}{c_1} [0_{2 \times 1} \quad I_{2 \times 2}] \in \mathbb{R}^{2 \times 3}, \quad (8)$$

$$D^m = \frac{1}{c_1} \begin{bmatrix} c_1 + c_2 + c_3 & -c_3 \\ c_3 & c_1 + c_2 + c_3 \end{bmatrix} \in \mathbb{R}^{2 \times 2}, \quad (9)$$

$x_k^m = [q_k, \dot{q}_k, \dot{q}_{k-1}]^T \in \mathbb{R}^3$, and $u_k^m = [V_k, V_{k-1}] \in \mathbb{R}^2$. The signal $n_k^m \in \mathbb{R}^2$ is zero-mean measurement noise with covariance $N^m = N^H + DN^D D^T$. The measurement noise covariance is computed directly on the hardware, and we describe our process in section 6.1. Note that the process and measurement states are not equal ($x^m \neq x^p$), and the following section builds an augmented state to resolve this discrepancy.

3.3. Complete estimator

Combining the process and measurement models, we write the linearized discrete-time dynamics of a single transmission-sensor system in the following form:

$$x_{k+1} = Ax_k + Bu_k + w_k \quad (10)$$

$$y_k = Hx_k + Du_k + n_k, \quad (11)$$

where $x_k = [(x_k^p)^T, \dot{q}_{k-1}^s, \dot{q}_{k-1}^l]^T \in \mathbb{R}^6$ is the state, $y_k = [V_k^{m,s}, V_k^{m,l}, V_{k-1}^{m,s}, V_{k-1}^{m,l}]^T \in \mathbb{R}^4$ is the measurement, $u_k = [(u_k^p)^T, (u_{k-1}^p)^T]^T \in \mathbb{R}^4$ is the input. Furthermore, $w_k \in \mathbb{R}^6$ and $n_k \in \mathbb{R}^4$ are the zero-mean process and measurement noises with covariances given by

$$W = \begin{bmatrix} W^p & 0 \\ 0 & 0 \end{bmatrix} \quad \text{and} \quad N = \begin{bmatrix} N^m & 0 \\ 0 & N^m \end{bmatrix}, \quad (12)$$

respectively. Finally, the system matrices are given by

$$A = \begin{bmatrix} A^p & 0_{4 \times 2} \\ [e_2, e_3]^T & 0_{2 \times 2} \end{bmatrix} \in \mathbb{R}^{6 \times 6}, \quad (13)$$

$$B = \begin{bmatrix} B^p & 0_{2 \times 2} \\ 0_{2 \times 2} & 0_{2 \times 2} \end{bmatrix} \in \mathbb{R}^{6 \times 4}, \quad (14)$$

$$H = \begin{bmatrix} 0 & h_{11}^m & 0_{1 \times 4} \\ 0_{1 \times 2} & h_{11}^m & 0_{1 \times 3} \\ 0_{1 \times 4} & h_{22}^m & 0 \\ 0_{1 \times 4} & 0 & h_{22}^m \end{bmatrix} \in \mathbb{R}^{4 \times 6}, \quad (15)$$

$$D = \begin{bmatrix} d_{11}^m & 0 & d_{12}^m & 0 \\ 0 & d_{11}^m & 0 & d_{12}^m \\ d_{21}^m & 0 & d_{22}^m & 0 \\ 0 & d_{21}^m & 0 & d_{22}^m \end{bmatrix} \in \mathbb{R}^{4 \times 4}. \quad (16)$$

Here h_{ij}^m and d_{ij}^m are ij th entries of H^m and D^m , respectively, and e_2 and e_3 are elementary unit vectors in \mathbb{R}^4 . Given this formulation, the infinite-horizon Kalman gain is computed off-line as $K = PH(HPH^T + R)^{-1} \in \mathbb{R}^{6 \times 4}$, where P is found by solving the discrete-time algebraic Ricatti equation [50]. The current state estimate is then given by

$$\hat{x}_k = A\hat{x}_{k-1} + Bu_{k-1} + K(y_k - H(A\hat{x}_{k-1} + Bu_{k-1}) - Du_k), \quad (17)$$

where the state is initialized to $\hat{x}_0 = 0$.

This simple update rule can be carried out independently for each transmission and only requires the addition of vectors \mathbb{R}^6 and multiplication of vectors in \mathbb{R}^6 by sparse matrices in $\mathbb{R}^{6 \times 6}$. Though this filter is currently implemented off-board, this method, because of its computational efficiency, can easily be implemented in real-time on the autonomous version of this robot [51].

4. Controller design

Similar to the complete estimator, the feedback controller is also independently derived for a transmission-sensor system. A subset of estimated actuator positions and velocities (\hat{x}_k^p) is used in a feedback controller designed as a linear-quadratic-regulator (LQR). LQR controllers have been used to stabilize both smooth and hybrid non-linear systems; for example, the time-varying LQR formulation (TVLQR, [52]) is often used to locally stabilize nonlinear systems about a given trajectory. Furthermore, LQR has been used to stabilize limit cycles for hybrid systems, both in full-coordinates using the jump-Ricatti equation [53] and in transverse-coordinates using a transverse linearization [54].

In this work, since each of HAMR's leg can exert forces greater than one body-weight [39], we can treat the relatively small contact forces as disturbances. Furthermore, since an LTI system provides an accurate representation of the transmission dynamics in air, we choose to use an infinite-horizon LQR controller. This controller minimizes the following cost function:

$$J = \sum_{k=0}^{\infty} (\hat{x}_k^p - x_k^0)^T Q (\hat{x}_k^p - x_k^0) + (u_k^p - u_0^p)^T R (u_k^p - u_0^p), \quad (18)$$

where $Q \succeq 0$ and $R \succ 0$ are symmetric matrices that penalize deviations from the fixed point (x_0^p, u_0^p) . We defined Q and R as diagonal matrices parameterized by three positive scalars (k_p, k_v , and k_u) that determine trade-offs between squared deviations in actuator position, velocity, and control voltage, respectively. The complete control law combines the LQR feedback rule with a feed-forward term ($u_k^f = u_0^p + u_k^t \in \mathbb{R}^2$):

$$u_k^p = u_k^f + L(x_k^r - \hat{x}_k^p). \quad (19)$$

Here $x_k^r \in \mathbb{R}^4$ is the reference state, $L = (R + B^T S B)^{-1} B^T S A \in \mathbb{R}^{2 \times 4}$ is the feedback matrix, and S is computed by solving the discrete-time algebraic Ricatti equation [50]. The resulting linear-quadratic-Gaussian (LQG) dynamical system is formulated by combining equation (17) with the control law given in equation (19).

Intuitively, the feed-forward term is equal to the nominal voltage (u_0^p) if the reference state is the fixed point. Furthermore, the control law in equation (19)

will stabilize the LQG system since Q and R are chosen to be positive-definite. In practice, the controller is used to track reference trajectories on the physical (nonlinear) legged robot, the control input (u_k^p) still acts to reduce the error, and ground reaction forces can be thought of as disturbances. We also augment the feed-forward term with a time varying component (u_k^t) that is computed via a trajectory optimization without ground contact (Note S3 (stacks.iop.org/BIB/14/056001/mmedia)). This term is similar to the nominal input for a TVLQR controller about a trajectory; however, the lack of ground contact modeling makes it more of a heuristic for improving the convergence rate and reducing steady-state error.

5. Bio-inspired trajectory selection

Using the estimation and control framework described in the previous two sections (sections 3 and 4), we are now able to track arbitrary leg trajectories subject to the dynamics of the transmission. We exploit this to expand on our previous work that explored the effect of gait and stride frequency on locomotion [37]. The major challenges that limited locomotion performance in our previous studies are:

- (1) High leg-slip (40%–45% ineffective stance) across all stride frequencies.
- (2) Increased body oscillations (in roll and pitch) in the body dynamics frequency range (20 Hz–40 Hz).
- (3) Departure from SLIP-dynamics [55] beyond the mechanically tuned operating point close to robot z-resonance (~ 10 Hz).
- (4) Fixed (open-loop) timing between vertical and fore-aft resulting in poor or backwards locomotion (e.g. when pronking at 10 Hz).

In this work, we postulate the following four specific hypotheses to understand the underlying mechanisms behind the challenges enumerated above. These hypotheses (described below) are motivated by relevant examples from recent scientific literature, and the application of these ideas to an dexterous insect-scale system across a wide range of stride frequencies is a contribution of this work. Ultimately, we hypothesize (H_0) that exploring the leg trajectories described below can reveal optimized shape control parameters that enable high-performance locomotion over the entire operating range of the robot, overcoming challenges observed in our previous research [37].

5.1. Hypothesis one (H_1)

Template models of legged locomotion, such as SLIP, have relied on a swing-leg retraction strategy for stabilizing sagittal plane locomotion [56–60]. These results have been supported by numerous experimental studies on bipedal running [61] in

humans [56, 62] and guinea fowls [8, 63], and on quadrupedal galloping in horses [64]. Expanding this approach, researchers have demonstrated an optimal retraction rate for perturbation rejection [65] and energy efficient locomotion [66]. Additionally, modeling and experimental results using large bio-inspired quadrupedal robots [65, 67] indicate that swing leg retraction can potentially mitigate the risk of slippage at heel-strike during rapid running. Therefore, we test the effect of varying leg retraction period on locomotion and hypothesize (H_1) that *increasing the leg retraction period reduces slipping and improves locomotion performance*.

5.2. Hypothesis two (H_2)

Upright-posture animals have been shown to modulate their normal force and vertical impulse to minimize body oscillations and maintain stable locomotion in the sagittal plane [68–71]. Similarly, studies in humans show that the above considerations are important for overcoming roll perturbations and achieving lateral stability [72, 73]. Robots employ these bio-inspired strategies [74–77] to stabilize hip height [78, 79] and control pitch oscillations [80, 81]. The underlying mechanisms either passively (mechanically) [82, 83] or actively modulate ground reaction forces [84] and impulses [85, 86]. We adapt this approach to minimize vertical, pitch, and roll body oscillations in the body dynamics frequency range, and we hypothesize (H_2) that *increasing input lift energy, especially in the body dynamics frequency range, increases detrimental body oscillations and reduces locomotion performance*.

5.3. Hypothesis three (H_3)

Animals of varying size and morphology [87] use energy storage and exchange mechanisms [7, 88, 89] during locomotion [10]. Numerous models explain these ubiquitous underlying mechanisms, the most popular of which is the SLIP model [55, 90–92]. Furthermore, the implications of relative stiffness [87, 93] on locomotion speed [89, 94–96], stability [97, 98] and economy [88, 99–101] are well documented across body sizes. Based on this understanding, we hypothesize (H_3) that *increasing effective leg stiffness allows for greater energy storage and return (SLIP-like dynamics) and improves performance at higher stride frequencies*.

5.4. Hypothesis four (H_4)

During running the body decelerates during the first half of stance, and accelerates into flight during the second half of the stance. Studies have shown that relative timing of vertical and fore-aft leg motions is important in achieving a pattern of deceleration and acceleration that results in effective locomotion [102, 103]. Given that time-of-flight will change as a function of stride frequency (due to body resonances), we hypothesize (H_4) that *the timing between the*

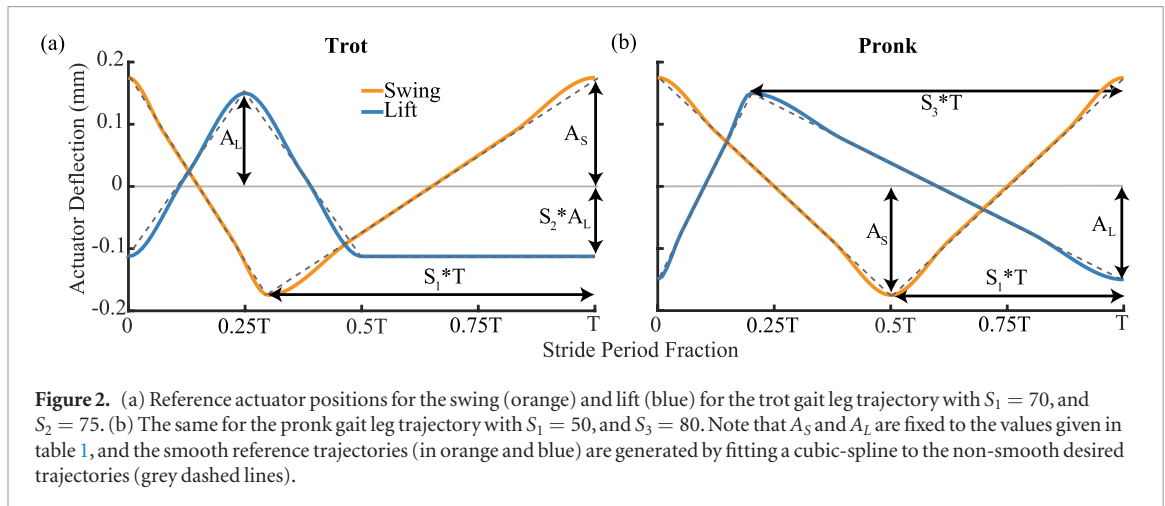


Table 1. Heuristic trajectory design parameters.

Parameters	Description	Trot gait	Pronk gait
A_S	Swing amplitude	175 μm	150 μm
A_L	Lift amplitude	175 μm	150 μm
T	Stride period ($\frac{1}{\text{frequency}}$)	$\in [\frac{1}{50}, \frac{1}{40}, \frac{1}{30}, \frac{1}{20}, \frac{1}{10}]$ ms	$\in [\frac{1}{50}, \frac{1}{40}, \frac{1}{30}, \frac{1}{20}, \frac{1}{10}]$
S_1	Shape control one	Leg retraction period (% T) $\in [50, 60, 70, 80]$	Leg retraction period (% T) $\in [50, 60, 70, 80]$
S_2	Shape control two	Maximum leg adduction (% A_L) $\in [-75, -50, -25, 0, 25]$	N/A
S_3	Shape control three	N/A	Leg adduction period (% T) $\in [20, 35, 50, 65, 80]$

vertical and fore-aft leg motions that results in the best performance varies as a function of stride frequency.

5.5. Trajectory design

We distill these four hypotheses into parametric leg trajectories for the trot (figure 2(a)) and pronk (figure 2(b), supplementary video S4) gait, respectively. Each trajectory is defined by five parameters described in table 1. Here, the swing (A_S) and lift (A_L) actuator amplitudes are held constant, T controls the stride frequency, and the shape parameters S_1 , S_2 , and S_3 vary as described below. For both parametric trajectories, we address H_1 by maintaining a constant speed during leg retraction and vary the leg retraction period as a trajectory shape control parameter S_1 . For the trot gait, we also vary the maximum leg adduction via the shape parameter S_2 . This modification directly varies the net energy imparted to the lift (z) motion addressing H_2 . In addition S_2 also modulates leg stiffness (see figure S2 and Note S3) addressing H_3 . Finally, we vary the leg adduction period as the trajectory shape control parameter S_3 for the pronk gait. This modification, coupled with S_1 from above, varies the timing between the vertical and fore-aft leg motions addressing H_4 .

6. Experimental design, methods and metrics

This section first describes the calibration conducted before running experiments (section 6.1). We then

describe the experimental procedures and apparatus for evaluating the estimator (derived in section 3) and controller (derived in section 4) performance, and for exploring the heuristic leg trajectories (developed in section 5). Finally, we define a number of locomotion performance metrics in section 6.5 that are used to quantify the effects of varying leg trajectory shape in section 8.

6.1. Calibration

A calibration was performed for each robot and single-leg before conducting all experiments. The measurement noise covariances N^H and N^D were computed from mean-subtracted measurements of V^m and V , respectively, with $u^a = 0$. These means (corresponding to an initial offset) were also subtracted from subsequent measurements of V^m and V . The velocity scaling coefficients (α) from the mechanical current (mA) to tip velocity (mm s^{-1}) were computed for each actuator over the range of operating frequencies. The coefficient for each actuator was set to the value that minimized the squared-error between the mechanical current (i_m , equation (2)), and corresponding ground-truth leg velocity.

6.2. Estimator validation

Estimator validation was conducted on a single-leg (figure 3(a)) using the architecture shown in figure 3(c). Note that control gains (L) were set to zero.

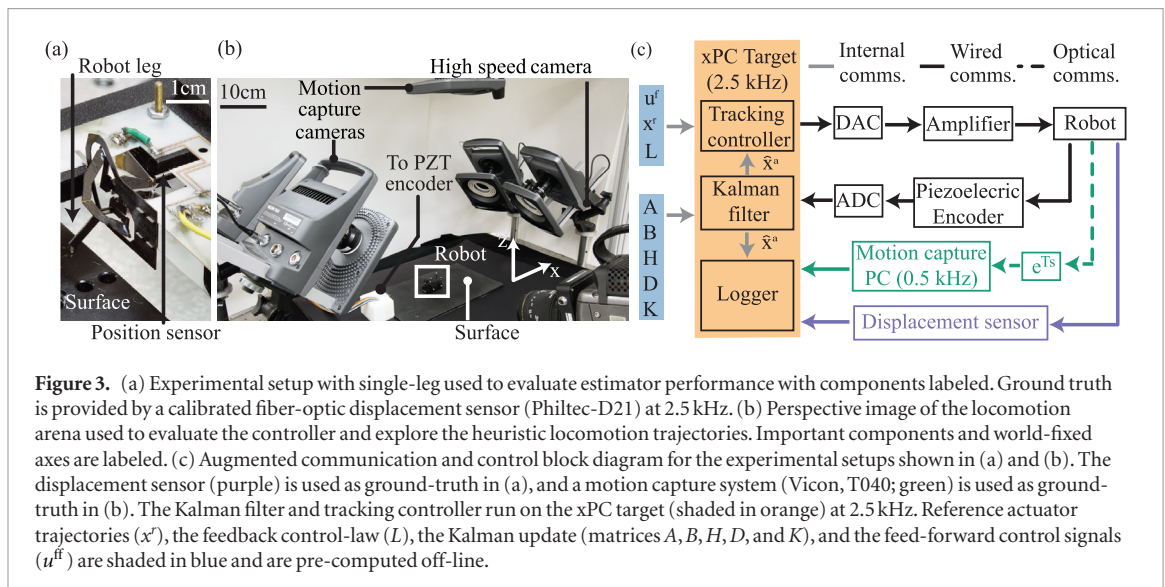


Figure 3. (a) Experimental setup with single-leg used to evaluate estimator performance with components labeled. Ground truth is provided by a calibrated fiber-optic displacement sensor (Philtec-D21) at 2.5 kHz. (b) Perspective image of the locomotion arena used to evaluate the controller and explore the heuristic locomotion trajectories. Important components and world-fixed axes are labeled. (c) Augmented communication and control block diagram for the experimental setups shown in (a) and (b). The displacement sensor (purple) is used as ground-truth in (a), and a motion capture system (Vicon, T040; green) is used as ground-truth in (b). The Kalman filter and tracking controller run on the xPC target (shaded in orange) at 2.5 kHz. Reference actuator trajectories (x^r), the feedback control-law (L), the Kalman update (matrices A , B , H , D , and K), and the feed-forward control signals (u^f) are shaded in blue and are pre-computed off-line.

Sinusoidal input signals (u^f) were generated at 2.5 kHz using a MATLAB xPC environment (MathWorks, R2015a), and were supplied to the single-leg through a four-wire tether. The Kalman filter (defined in section 3) estimated actuator position and velocity from the voltage measurements provided by two piezoelectric encoders at 2.5 kHz. Finally, ground truth swing and lift actuator position measurements were provided by calibrated fiber-optic displacement sensors (Philtec-D21) at the same rate.

We measured estimator performance at stride frequencies of 10, 20, 30, 40, and 50 Hz both in-air and with ground-contact. Ground contact was achieved by positioning a surface at the neutral position of the leg for the duration of the trial. Estimation error for a single actuator was quantified as \bar{E}_{est} , which is the N -cycle mean of the RMS error between the estimated actuator position and ground-truth measurements normalized by the peak-to-peak amplitude of the ground-truth measurements.

We also quantified estimator performance on a full-robot at frequencies of 10, 20, 30, 40, and 50 Hz using the locomotion arena shown in figure 3(b) to determine if the estimator could also be used to accurately predict leg positions (l^x, l^z). These trials were also conducted using the architecture shown in figure 3(c) with sinusoidal inputs and the control gains set to zero. Five motion capture cameras (Vicon T040) tracked the position and orientation of the robot at 500 Hz with a latency of 11 ms. A custom C++ script using the Vicon SDK enabled tracking of the leg tips in the body-fixed frame. We used a model of the transmission kinematics to map the estimated actuator position to l^x and l^z , and these estimates were compared against ground truth leg position measurements provided by the motion-capture system. Performance was quantified using \bar{E}_{est} .

6.3. Controller validation

We also quantified controller performance on an entire robot at frequencies of 10, 20, 30, 40, and 50 Hz.

Experiments were performed both in air and in the presence of ground contact using the experimental arena shown in figure 3(c) and described in section 6.2. To determine the effectiveness of the controller performance, we quantified tracking error using \bar{E}_{cont} , defined as the N -cycle mean of the RMS error between the estimated and desired actuator position measurements normalized by the peak-to-peak amplitude of the desired actuator position.

6.4. Leg trajectory exploration

We also performed 400 closed-loop trials to evaluate HAMR's performance when using the two classes of heuristic leg trajectories (section 5). These experiments used two robots whose floating-base natural frequencies are characterized in figure S1 using methods described by Goldberg *et al* [37]. Two hundred trials were conducted on each robot with 100 trials for each class of heuristic leg trajectory. Each subset of one hundred trials enumerated all possible combinations of stride period (T) and shape parameters (S_1, S_2 , and S_3). The 400 trials were all conducted in the locomotion arena described above. Since both robots showed similar performance, we averaged the data to compute locomotion metrics (section 6.5).

6.5. Locomotion performance metrics

We quantified the performance of the robot using the three performance metrics described below.

6.5.1. Normalized per cycle speed (ν)

This is a measure of the speed of the robot (ν) during locomotion. It is defined as the ratio of speed achieved per step to the kinematic step length and is computed as

$$\nu = \frac{v}{L_s n f}, \quad (20)$$

where $L_s = 4.7$ mm is the kinematic step length, n is the number of steps per stride for a given gait

($n_{\text{rot}} = 2, n_{\text{prnk}} = 1$) and $f = \frac{1}{T}$ is the stride frequency. Intuitively, $\nu = 1$ is the expected forward speed assuming ideal kinematic locomotion, and $\nu > 1$ suggests that the robot is utilizing dynamics favorably to increase its stride length beyond the kinematic limits.

6.5.2. Step effectiveness (σ)

This is a measure of the robot leg slippage during locomotion. It is defined for each leg as one minus the ratio of leg-slip to the kinematic step length. We consider leg-slip to be the total distance a single leg travels in the direction opposite to the robot heading in the world frame. We present an average value for all four legs computed as

$$\sigma = 1 - \frac{1}{4L_s} \sum_{i=1}^4 \int_{\zeta} |v_x^i(t)| dt, \quad (21)$$

where v_x^i is the x -velocity of the i th leg in the world-fixed frame, and ζ is the set of times within a step for which v_x^i is in the opposite direction as the robot heading. Intuitively, $\sigma = 1$ indicates no slipping while $\sigma = 0$ indicates continuous slipping (i.e. no locomotion of the robot).

6.5.3. Locomotion economy (ϵ)

This is a measure of the the robot's COT [104]. This is defined as the ratio of the robot's mechanical output power to the total electrical power consume and is quantified as:

$$\epsilon = \frac{mgv_x}{\sum_{i=1}^8 \frac{1}{T} \int_0^T i^m(t) V^m(t) dt}, \quad (22)$$

where $m = 1.43$ g is the mass of the robot and $g = 9.81$ m s⁻² is the acceleration due to gravity. Intuitively, lower values of ϵ indicate poor conversion of the input electrical power into mechanical output, suggesting ineffective locomotion performance.

6.6. Open-loop control trajectory comparison

Finally, we also conducted the following open-loop experiments to serve as a baseline for the experiments described in section 6.4.

6.6.1. Coupled sinusoids

The RMS amplitude for each sinusoidal drive voltage was equal to the average of the RMS voltages delivered to all eight actuators during the fastest trial at a particular stride period. This control experiment did not discriminate between voltages delivered to the lift and swing DOFs and is therefore referred to as the *coupled configuration*.

6.6.2. Decoupled sinusoids

The RMS amplitude for the four lift (and four swing) actuators was equal to the average RMS voltage delivered to the lift (and swing) actuators during the fastest trial at a particular stride period, respectively.

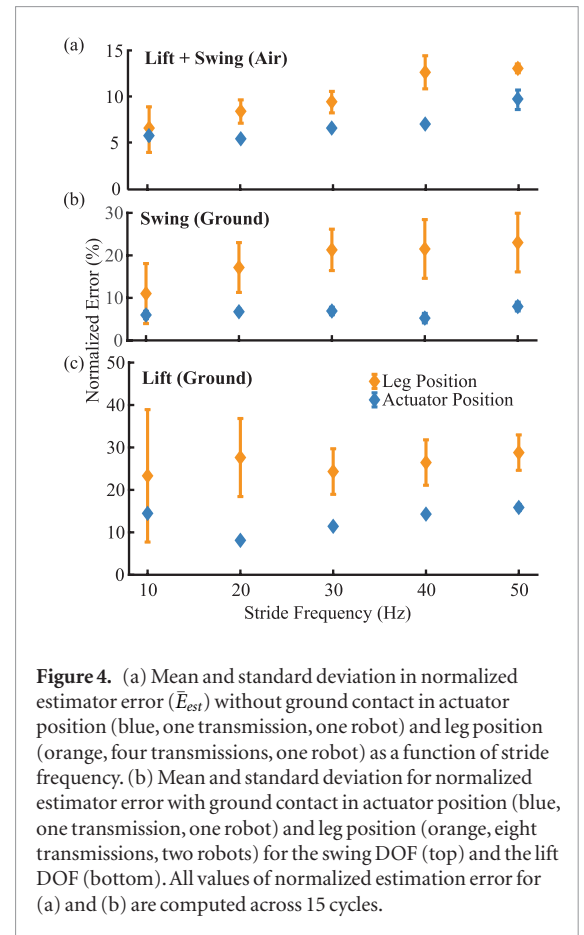


Figure 4. (a) Mean and standard deviation in normalized estimator error (\bar{E}_{est}) without ground contact in actuator position (blue, one transmission, one robot) and leg position (orange, four transmissions, one robot) as a function of stride frequency. (b) Mean and standard deviation for normalized estimator error with ground contact in actuator position (blue, one transmission, one robot) and leg position (orange, eight transmissions, two robots) for the swing DOF (top) and the lift DOF (bottom). All values of normalized estimation error for (a) and (b) are computed across 15 cycles.

The voltages delivered to the lift and swing actuators were individually computed, and therefore, this is referred to as the *decoupled configuration*.

7. Estimator and controller performance

This section summarizes our results related to the quantification of estimator and controller performances. In particular, we evaluate the accuracy of both the linear approximation (described in section 3.1) of the transmission model and the treatment of ground contact as a perturbation (described in section 4).

7.1. Estimator

The performance of the estimator is shown in figure 4 with estimation errors for a representative trial in air and on the ground shown in supplementary figure S4. For the trials in air (figure 4(a)), the mean normalized estimation error in actuator position ranges from 5% at 10 Hz to 10% at 50 Hz. These numbers indicate reasonably accurate estimation in air, confirming the accuracy of the sensor measurements and validity of the linear approximation of the non-linear transmission dynamics. The error in leg position is higher than actuator position error and ranges from 6% at 10 Hz to 15% at 50 Hz, and we suspect this is due to inaccuracies in the modeled transmission kinematics.

Similarly, actuator position error (blue) is low when subject to approximated ground-contact. The normalized swing (figure 4(b)) and lift (figure 4(c)) actuator position errors are between 5%–10% and 8%–16%, respectively. We suspect that the lift position errors are higher because the process model does not capture the effect of (1) perturbations from ground contact and (2) serial compliance between the actuator and mechanical ground [105]. Nevertheless, these errors are still relatively small, indicating that the Kalman filter effectively averages the sensor measurement that registers contact with a linear predication that does not drift.

Finally, we find that the normalized leg position error (orange) with ground contact is higher than normalized actuator position-error (blue). The leg- x error (l_x , figure 4(b)) ranges from 11% to 24%, and leg- z error ranges (l_z , figure 4(c)) from 23% to 29%. The most likely cause of this is the serial compliance in the transmission—a common problem in flexure-based devices [39, 105]. This serial compliance alters the kinematics of the transmission by effectively adding un-modeled DOFs between the actuators and leg and changes the assumed one-to-one mapping between actuator and leg positions.

7.2. Controller

The performance of the controller is shown in figure 5 with tracking errors for a representative trial in air and on the ground shown in supplementary figure S5. For the trials in air (figure 4(a)), the mean normalized estimation error in actuator position increases from 5% at 10 Hz to 15% at 50 Hz for the swing DOF and from 5% at 10 Hz to 11% at 50 Hz for the lift DOF. This demonstrates the linear approximation of the transmission dynamics is sufficient for control in the absence of ground contact. Moreover, the normalized tracking error (figure 5(b)) for both the swing and lift DOFs when running is also small, and it increases from 6% at 10 Hz to 16% at 50 Hz. This indicates that treating ground contact as a perturbation does not significantly reduce tracking performance. Finally, a likely reason for the increase in tracking error as a function of stride frequency is that the high-frequency components in the heuristically designed leg trajectories become harder to track as they approach the robot's transmission resonant frequencies (between 80 Hz–100 Hz, [106]).

8. Locomotion performance

The average value for each locomotion performance metric described in section 6.5 are plotted as a function of the shape control parameters (table 1) at all five tested stride frequencies (10 Hz–50 Hz) in figure 6. We first summarize the robot's locomotion performance for the trot gait, validate hypotheses H_1 and H_3 , and invalidate hypothesis H_2 . We then summarize

performance for the pronk gait, refute hypothesis H_1 , and validate hypothesis H_4 .

8.1. Trot gait performance summary

As shown in figure 6(a), we are able to achieve locomotion over a wide range of speeds (43 mm s^{-1} – 278 mm s^{-1} or 0.95 BL s^{-1} – 6.17 BL s^{-1} , $n = 200$ trials, $N = 2$ robots) by varying stride frequency and the shape control parameters. We also measure step effectiveness for the above gaits ranging from 0.25 to 0.91 (figure 6(a)). In addition, we find that locomotion economy (figure 6(a)) varies nearly four-fold (0.08–0.30) and shows a strong dependence on shape control parameters both within and across frequencies. The resulting cost of transport (COT) values range from 3.33–13.14, and are some of the lowest measured on this platform [35, 37]. Finally, we note that COT increases with frequency while maintaining a trot, supporting the hypothesis that the preferred gait varies as a function of running speed [107]. The best and worst performing trials are visualized in supplementary video S2.

8.2. H_1 —trot gait

For all stride frequencies, a higher leg retraction period results in increased step effectiveness (C, figure 6(a)). Leg retraction period, however, is only positively correlated with per-cycle velocity at high stride frequencies (A, figure 6(a)). Finally, a higher leg retraction period results in lower locomotion economy at all stride frequencies (E, figure 6(a)). These trends support our initial hypothesis (H_1) that increasing leg retraction period increases step effectiveness by decreasing slipping. However, step effectiveness is only a good predictor of speed at high stride frequencies (D2, figure 6(a)), and the two are uncorrelated at low stride frequencies (D1, figure 6(a)). This is because the body dynamics (figure S1) have a dominating effect on speed at lower stride frequencies. These dynamics, however, are attenuated at higher stride frequencies, and, therefore, speed in those regimes is largely determined by the magnitude of foot slipping [37]. This negative correlation between locomotion economy and leg retraction period also indicates that the energetic cost of tracking the high-velocity leg protraction might offset the benefit of mitigating leg slip. Finally, our results corroborate previous findings [65–67] that imply the existence of preferred values of leg retraction period that minimize foot slippage and economy, respectively. Moreover, we find that these values are a function of the stride-frequency dependent dynamics of the robot.

8.3. H_2 and H_3 —trot gait

For all stride frequencies, higher maximum leg adduction results in both higher step effectiveness (C, figure 6(a)) and higher per-cycle velocity (B, figure 6(a)). These trends refute our initial hypothesis (H_2) that increasing the maximum leg adduction

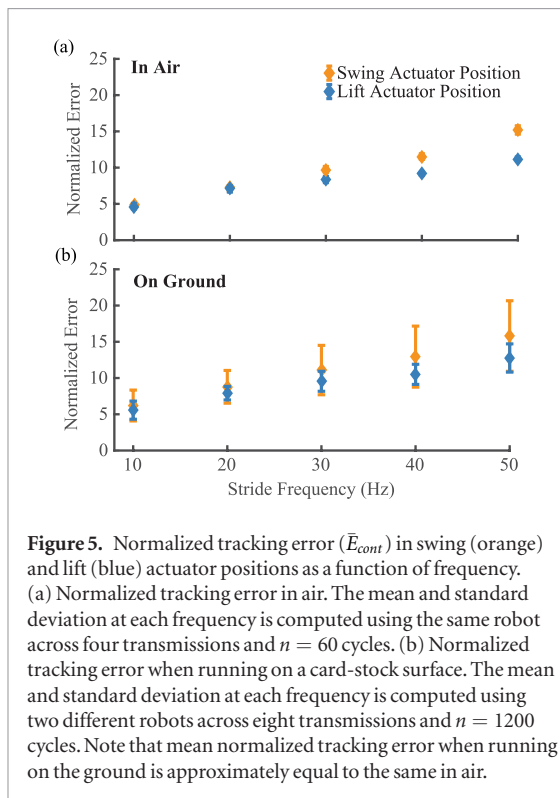


Figure 5. Normalized tracking error (\bar{E}_{cont}) in swing (orange) and lift (blue) actuator positions as a function of frequency. (a) Normalized tracking error in air. The mean and standard deviation at each frequency is computed using the same robot across four transmissions and $n = 60$ cycles. (b) Normalized tracking error when running on a card-stock surface. The mean and standard deviation at each frequency is computed using two different robots across eight transmissions and $n = 1200$ cycles. Note that mean normalized tracking error when running on the ground is approximately equal to the same in air.

reduces locomotion performance in terms of speed. It is likely that higher maximum leg adduction results in increased normal and frictional support, both reducing slipping and improving forward speed.

Furthermore, increasing maximum leg adduction increases the effective leg stiffness (see figure S2 and Note S3) and this likely allows for greater energy storage and return, facilitating faster locomotion and supporting our initial hypothesis (H_3). We suspect this is because increasing maximum leg adduction increases the relative leg stiffness for HAMR by a factor of ~ 2 from 4.3 with zero maximum leg adduction [37]. The robot's relative stiffness now approaches what is observed in animals (~ 10 [87]) resulting in effective SLIP-like locomotion [55]. However, higher maximum leg adduction results in lower locomotion economy across all stride frequencies (E, figure 6(a)). This suggests that increasing maximum leg adduction increases power consumption; however, this increase does not enable proportional gains in output mechanical power (i.e. forward speed) and results in less effective locomotion.

8.4. Pronk gait performance summary

We find that modulating the timing between vertical and fore-aft leg motions enables locomotion over a wide range of speeds (-176 mm s^{-1} – 236 mm s^{-1} or -3.91 BL s^{-1} – 5.24 BL s^{-1} , $n = 200$ trials, $N = 2$ robots; blue contours in figure 6(b)) in both forward and reverse directions. The fastest trials ($\nu > 1$) are highly dynamic with long aerial and short stance phases. We also observe that step effectiveness varies from 0.01 to 0.76 (orange contours, figure 6(b)). In addition,

we find that locomotion economy (green contours, figure 6(b)) varies nearly fifteen-fold (0.02–0.24). The resulting COT values (4.21–64.84) span the range from being among the lowest measured for this platform to some of the highest at each frequency. Finally, we note that actuator per-cycle energy consumption is independent of the stride frequency and the gait shape control parameters, and, as a consequence, the contour maps of ϵ mirror that of ν . The best and worst performing trials are visualized in supplementary video S3.

8.5. H_1 —pronk gait

We find that the lowest leg retraction period results in the highest per-cycle velocity (F, figure 6(b)) and locomotion economy (H, figure 6(b)) across all stride frequencies. This matches our intuition that rapid leg swing retraction during stance is key to maximizing the net forward impulse imparted to the robot. Furthermore, we do not see a clear trend in the dependence of step effectiveness on leg retraction period (G, figure 6(b)); however, we again see that step effectiveness is a good predictor of normalized per-cycle speed at higher stride frequencies. These trends refute our initial hypothesis H_1 that increasing leg retraction period reduces leg slip and therefore results in improved performance.

8.6. H_4 —pronk gait

A high leg adduction period and low swing retraction period results in fast forward locomotion (F, figure 6(b)), high step effectiveness (G, figure 6(b)), and high locomotion economy (H, figure 6(b)) for stride frequencies from 20 Hz–50 Hz. Similarly, a low leg adduction period and high leg retraction period results in fast backwards (enclosed by a purple polygon) locomotion and high locomotion economy. Finally, intermediate values of leg adduction (independent of leg retraction) result in ineffective locomotion. This supports our initial hypothesis (H_4) that the timing between vertical and fore-aft leg motions is crucial in determining locomotion performance and direction, and matches similar observations from previous studies [102, 103]. In contrast, we observe a reversal in the trends described above (I, figure 6(b)) at a stride frequency of 10 Hz where the robots mechanical z-resonance results in long flight phases that favor a shorter leg adduction period.

9. Effective locomotion performance across dynamic regimes

We analyze the best performing trials (figure 7) to test our final hypothesis (H_0) that closed-loop trajectory modulation enables high-performance locomotion across stride frequencies. Using speed as the primary metric to facilitate a comparison with previous results from [37], we define the best performing trial as the one with the highest normalized per cycle speed (ν)

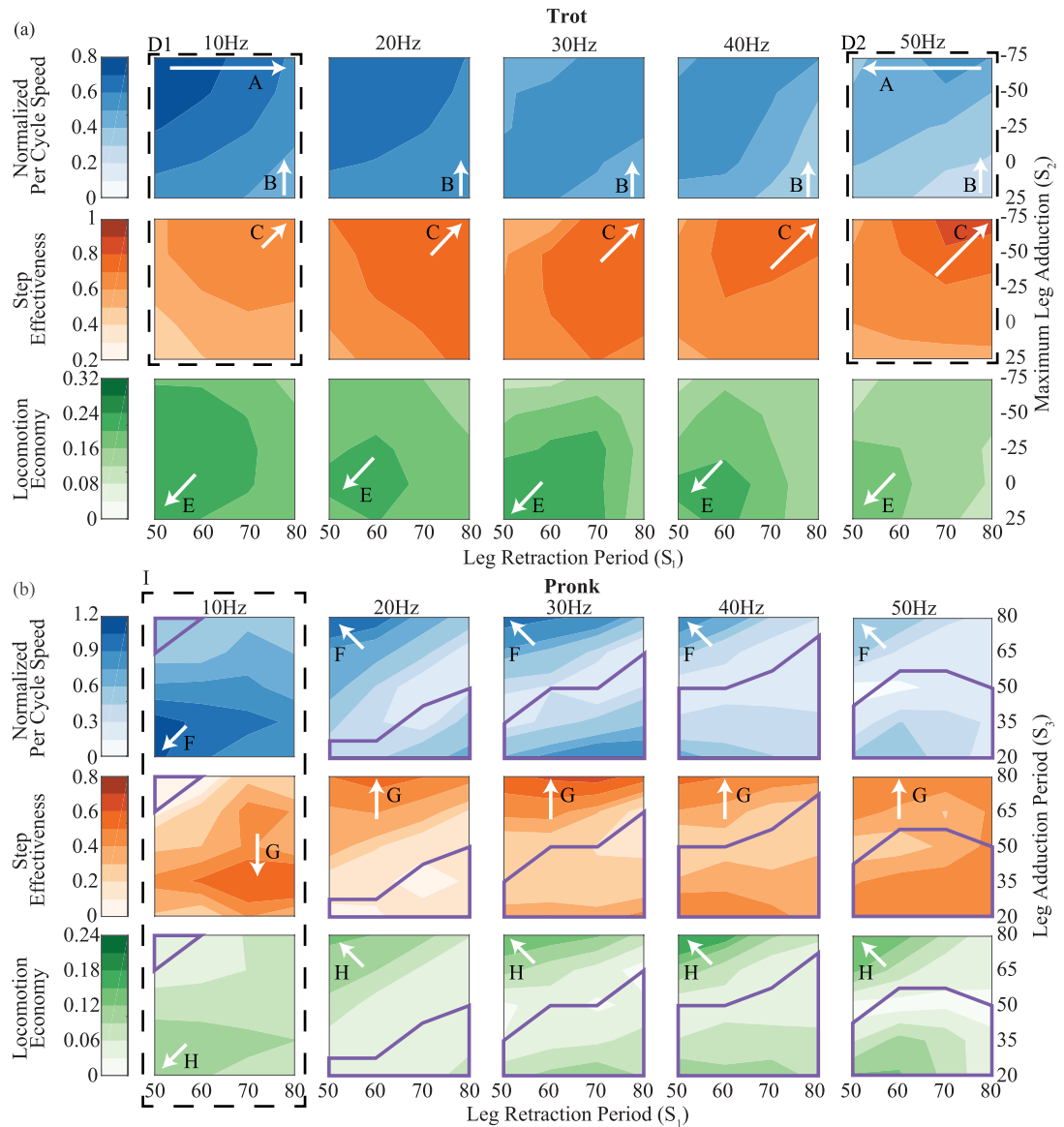


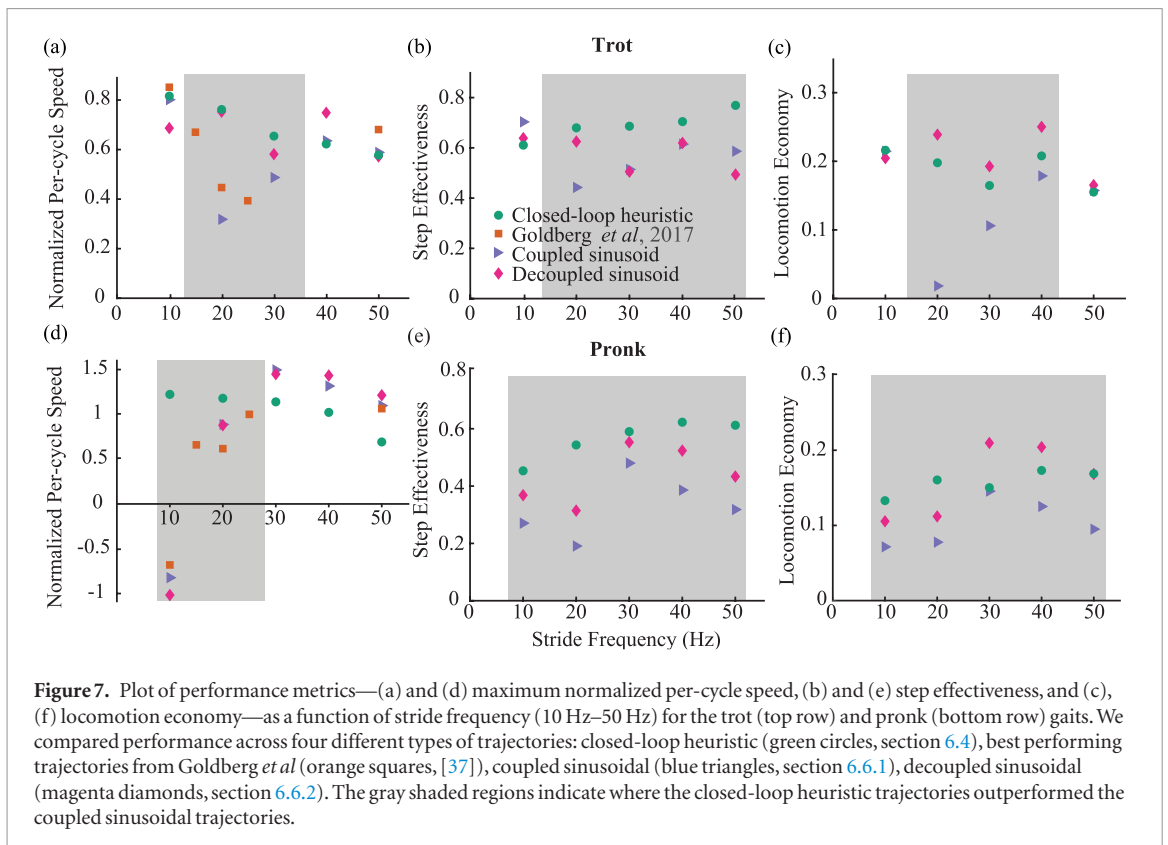
Figure 6. Contour plots depict the effect of the trajectory parameters, S_1 (x -axis) and S_2 (y -axis), on locomotion performance quantified by normalized per-cycle speed (blue), stride effectiveness (orange) and locomotion economy (green) as a function of stride frequency (10 Hz–50 Hz). (a) For the trot gait, the trajectory parameters are Leg Retraction Period (x -axis) and maximum leg adduction (y -axis). (b) For the pronek gait, the same are Leg Retraction Period (x -axis) and Leg Adduction Period (y -axis). The purple polygons indicate regions where locomotion was backward. Labels A–H refer to points of specific interest and are discussed in the text in section 8.

at each frequency for the trot and pronek, respectively. However, we also plot step effectiveness (ϵ) and locomotion economy (σ) for the best performing trials to consider multi-dimensional robot performance.

For the trot gait, we find that closed-loop heuristic trajectories allow the robot to maintain high speed locomotion across all stride frequencies (figure 7(a)). This is in contrast with the open-loop results from [37] and the coupled sinusoidal trajectories (section 6.6.1) where the robot suffers from poor performance in intermediate frequency regimes (15 Hz–35 Hz, supplementary video S1). However, we find that there is minimal difference in robot speed when using either the closed-loop heuristic leg trajectories or the decoupled sinusoidal trajectories (section 6.6.2). A similar trend is observed with locomo-

tion economy (figure 7(c)); however, the closed-loop heuristic trajectories enable higher step effectiveness at all stride frequencies greater than 10 Hz (figure 7(b)). These results suggest that, while the shape of leg trajectories is important for effective locomotion using the trot gait in the body dynamics regime (15 Hz–35 Hz), the distribution of energy between the leg vertical and fore-aft motion achieved via leg shape modulation is the significant consideration at operating conditions where the dynamics are neither mechanically tuned (10 Hz) nor attenuated (40 Hz–50 Hz).

Similarly, we also find that closed-loop heuristic trajectories allow the robot to maintain speed across all stride frequencies (figure 7(d)) when using a pronek gait. This is in contrast with the open-loop results from [37], the coupled sinusoidal trajectories, and



the decoupled sinusoidal trajectories where the robot suffers from poor performance between 5 Hz–25 Hz (supplementary video S1). On the other hand, closed-loop heuristic trajectories enable higher step effectiveness (figure 7(e)) and locomotion economy (figure 7(f)) across all stride frequencies compared to coupled input matched open-loop trajectories. This validates hypothesis H_0 , indicating that leg trajectory modulation enables high performance locomotion across stride frequencies.

10. Conclusion and future work

We have presented a computationally efficient framework for proprioceptive sensing and control of leg trajectories on a quadrupedal microrobot. We used this capability to explore two parametric leg trajectories designed to test a series of hypotheses investigating the influence of leg slipping, stiffness, timing, and energy on locomotion performance. This parameter sweep resulted in an experimental performance map that allowed us to select control parameters and determine a leg trajectory that maximized performance at a desired gait and stride frequency. Using these parameters, we recovered effective performance over a wide range of stride frequencies, achieving locomotion that is robust to perturbations from the robot's body dynamics [108].

Specifically, for the trot gait, we demonstrated that maximizing robot speed depends on minimizing slipping at high stride frequencies and leveraging favorable dynamics at low and intermediate stride frequencies. We found that the mechanism for doing either

was modulating leg trajectory shape, and consequently, input energy. In addition, we were able to increase energy storage and return by modulating leg stiffness, which resulted in faster locomotion. Furthermore, we found that leg timing determined performance for the prong gait and allowed for rapid locomotion in the forward or backwards directions.

As potential next steps towards improving the robot's state estimation, we plan to explicitly address the hybrid nature of the robot's underlying dynamics. Such an effort would require an appropriate contact sensor and a modification of the current estimation and control framework, and in principle could result in improved tracking performance. Moreover, we aim to use this low-level controller in conjunction with the trajectory optimization scheme described by Doshi *et al.* [109] to design feasible leg trajectories that optimize a given cost (e.g. speed, COT, etc) at a particular operating condition. This can automate the challenging task of designing appropriate leg trajectories for a complex legged system and result in better locomotion performance. Finally, we can use this controller to ensure accurate tracking of the leg trajectories during a variety of locomotion modalities including swimming [110] or climbing [111] with HAMR.

In addition to the planning and control efforts discussed above, the small footprint and mass of the sensors combined with the computational efficiency of the estimation and control scheme makes our approach suitable for future implementation on the autonomous version of HAMR [51]. We can also use the results from this work to inform future mechanical design decisions. For example, increasing the

transmission resonant frequencies [106] can increase control authority and enable improved leg trajectory control at stride frequencies higher than those tested in this work (>50 Hz). Ultimately, our results suggest that HAMR could be a strong candidate platform for systematically testing hypotheses about biological locomotion such as the effect of varying leg trajectories on locomotion [112].

Acknowledgments

Thank you to all members of the Harvard Microrobotics and Agile Robotics Laboratories for invaluable discussions. This work is partially funded by the Wyss Institute for Biologically Inspired Engineering. In addition, the prototypes were enabled by equipment supported by the ARO DURIP program (award #W911NF-13-1-0311).

ORCID iDs

Neel Doshi  <https://orcid.org/0000-0001-7011-0836>
Kaushik Jayaram  <https://orcid.org/0000-0002-6958-7650>

References

- Manton SM 1977 *The Arthropoda: Habits, Functional Morphology and Evolution* (Oxford: Oxford University Press)
- Gatesy S and Biewener A 1991 Bipedal locomotion: effects of speed, size and limb posture in birds and humans *J. Zool.* **224** 127–47
- Geyer H, Seyfarth A and Blickhan R 2006 Compliant leg behaviour explains basic dynamics of walking and running *Proc. R. Soc. B* **273** 2861–7
- Kenning M, Müller C H and Sombke A 2017 The ultimate legs of Chilopoda (Myriapoda): a review on their morphological disparity and functional variability *PeerJ* **5** e4023
- Daley M A and Biewener A A 2003 Muscle force-length dynamics during level versus incline locomotion: a comparison of *in vivo* performance of two guinea fowl ankle extensors *J. Exp. Biol.* **206** 2941–58
- Birn-Jeffery A V, Hubicki C M, Blum Y, Renjewski D, Hurst J W and Daley M A 2014 Do not break a leg: running birds from quail to ostrich prioritise leg safety and economy on uneven terrain *J. Exp. Biol.* **217** 3786–96
- McMahon T A 1985 The role of compliance in mammalian running gaits *J. Exp. Biol.* **115** 263–82
- Daley M A and Biewener A A 2006 Running over rough terrain reveals limb control for intrinsic stability *Proc. Natl Acad. Sci.* **103** 15681–6
- Wilshin S, Reeve M A, Haynes G C, Revzen S, Koditschek D E and Spence A J 2017 Longitudinal quasi-static stability predicts changes in dog gait on rough terrain *J. Exp. Biol.* **220** 1864–74
- Dickinson M H, Farley C T, Full R J, Koehl M, Kram R and Lehman S 2000 How animals move: an integrative view *Science* **288** 100–6
- Gorb S N 1995 Design of the predatory legs of water bugs (Hemiptera: Nepidae, Naucoridae, Notonectidae, Gerridae) *J. Morphol.* **223** 289–302
- Jayaram K, Mongeau J-M, Mohapatra A, Birkmeyer P, Fearing R S and Full R J 2018 Transition by head-on collision: mechanically mediated manoeuvres in cockroaches and small robots *J. R. Soc. Interface* **15** 20170664
- Yang E, Son J H, Lee S-I, Jablonski P G and Kim H-Y 2016 Water striders adjust leg movement speed to optimize takeoff velocity for their morphology *Nat. Commun.* **7** 13698
- Jayaram K and Full R J 2016 Cockroaches traverse crevices, crawl rapidly in confined spaces, and inspire a soft, legged robot *Proc. Natl Acad. Sci.* **113** E950–7
- Sakagami Y, Watanabe R, Aoyama C, Matsunaga S, Higaki N and Fujimura K 2002 The intelligent ASIMO: system overview and integration *IEEE/RSJ Int. Conf. on Intelligent Robots and Systems* vol 3 (IEEE) pp 2478–83
- Hubicki C, Grimes J, Jones M, Renjewski D, Spröwitz A, Abate A and Hurst J 2016 Atrias: design and validation of a tether-free 3D-capable spring-mass bipedal robot *Int. J. Robot. Res.* **35** 1497–521
- Raibert M, Blankespoor K, Nelson G and Playter R 2008 Bigdog, the rough-terrain quadruped robot *IFAC Proc. Volumes* **41** 10822–5
- Seok S, Wang A, Chuah M Y M, Hyun D J, Lee J, Otten D M, Lang J H and Kim S 2015 Design principles for energy-efficient legged locomotion and implementation on the MIT Cheetah robot *IEEE/ASME Trans. Mechatronics* **20** 1117–29
- Semini C, Barasuol V, Goldsmith J, Frigerio M, Focchi M, Gao Y and Caldwell D G 2016 Design of the hydraulically-actuated, torque-controlled quadruped robot *IEEE/ASME Trans. Mechatronics* **PP** 1
- Hutter M, Gehring C, Bloesch M, Hoepflinger M A, Remy C D and Siegwart R 2012 Starleth, efficient and versatile locomotion *Adaptive Mobile Robotics* (Singapore: World Scientific) pp 483–90
- Kuindersma S, Deits R, Fallon M, Valenzuela A, Dai H, Permenter F, Koolen T, Marion P and Tedrake R 2016 Optimization-based locomotion planning, estimation, and control design for the atlas humanoid robot *Auton. Robots* **40** 429–55
- Saranli U, Buehler M and Koditschek D E 2001 Rhex: a simple and highly mobile hexapod robot *Int. J. Robot. Res.* **20** 616–31
- Birkmeyer P, Peterson K and Fearing R S 2009 Dash: a dynamic 16 g hexapedal robot *IEEE/RSJ Int. Conf. on Intelligent Robots and Systems* pp 2683–9
- Pierre R S and Bergbreiter S 2017 Gait exploration of sub-2 g robots using magnetic actuation *IEEE Robot. Autom. Lett.* **2** 34–40
- Dharmawan A G, Hariri H H, Soh G S, Foong S and Wood K L 2018 Design, analysis, and characterization of a two-legged miniature robot with piezoelectric-driven four-bar linkage *J. Mech. Robot.* **10** 021003
- Bailey S A, Cham J G, Cutkosky M R and Full R J 2001 Comparing the locomotion dynamics of the cockroach and a shape deposition manufactured biomimetic hexapod *Experimental Robotics VII* (Berlin: Springer) pp 239–48
- Kim S, Clark J E and Cutkosky M R 2006 Isprawl: design and tuning for high-speed autonomous open-loop running *Int. J. Robot. Res.* **25** 903–12
- Haldane D W and Fearing R S 2015 Running beyond the bio-inspired regime *IEEE Int. Conf. on Robotics and Automation* pp 4539–46
- Haldane D W, Plecnik M M, Yim J K and Fearing R S 2016 Robotic vertical jumping agility via series-elastic power modulation *Sci. Robot.* **1**
- Birkmeyer P, Gillies A G and Fearing R S 2011 Clash: climbing vertical loose cloth *IEEE/RSJ Int. Conf. on Intelligent Robots and Systems* pp 5087–93
- Birkmeyer P, Gillies A and Fearing R S 2012 Dynamic climbing of near-vertical smooth surfaces *IEEE/RSJ Int. Conf. on Intelligent Robots and Systems* pp 286–92
- Karydis K, Poulakakis I, Sun J and Tanner H G 2015 Probabilistically valid stochastic extensions of deterministic models for systems with uncertainty *Int. J. Robot. Res.* **34** 1278–95
- Nagabandi A, Yang G, Asmar T, Pandya R, Kahn G, Levine S and Fearing R S 2018 Learning image-conditioned dynamics models for control of underactuated legged millirobots *IEEE/RSJ Int. Conf. on Intelligent Robots and Systems* (IEEE) pp 4606–13
- Baisch A T, Ozcan O, Goldberg B, Ithier D and Wood R J 2014 High speed locomotion for a quadrupedal microrobot *Int. J. Robot. Res.* **33** 1063–82

- [35] Goldberg B, Doshi N, Jayaram K, Koh J S and Wood R J 2017 A high speed motion capture method and performance metrics for studying gaits on an insect-scale legged robot *IEEE/RSJ Int. Conf. on Intelligent Robots and Systems* pp 3964–70
- [36] Goldberg B, Doshi N and Wood R J 2017 High speed trajectory control using an experimental maneuverability model for an insect-scale legged robot *IEEE Int. Conf. on Robotics and Automation* pp 3538–45
- [37] Goldberg B, Doshi N, Jayaram K and Wood R J 2017 Gait studies for a quadrupedal microrobot reveal contrasting running templates in two frequency regimes *Bioinspir. Biomim.* **12** 046005
- [38] Jayaram K, Jafferis N, Doshi N, Goldberg B and Wood R J 2018 Concomitant sensing and actuation for piezoelectric microrobots *Smart Mater. Struct.* **27** 065028
- [39] Doshi N, Goldberg B, Sahai R, Jafferis N, Aukes D and Wood R J 2015 Model driven design for flexure-based microrobots *IEEE/RSJ Int. Conf. on Intelligent Robots and Systems* pp 4119–26
- [40] Jafferis N T, Smith M J and Wood R J 2015 Design and manufacturing rules for maximizing the performance of polycrystalline piezoelectric bending actuators *Smart Mater. Struct.* **24** 065023
- [41] Karpelson M, Wei G-Y and Wood R J 2012 Driving high voltage piezoelectric actuators in microrobotic applications *Sensors Actuators A* **176** 78–89
- [42] Stephens B J 2011 State estimation for force-controlled humanoid balance using simple models in the presence of modeling error *IEEE Int. Conf. on Robotics and Automation* (IEEE) pp 3994–9
- [43] Bloesch M, Hutter M, Hoepflinger M A, Leutenegger S, Gehring C, Remy C D and Siegwart R 2013 State estimation for legged robots—consistent fusion of leg kinematics and IMU *Robotics* **17** 17–24
- [44] Singh S P and Waldron K J 2007 A hybrid motion model for aiding state estimation in dynamic quadrupedal locomotion *Proc. IEEE Int. Conf. on Robotics and Automation* (IEEE) pp 4337–42
- [45] Koval M C, Pollard N S and Srinivasa S S 2015 Pose estimation for planar contact manipulation with manifold particle filters *Int. J. Robot. Res.* **34** 922–45
- [46] Lowrey K, Kolev S, Tassa Y, Erez T and Todorov E 2014 Physically-consistent sensor fusion in contact-rich behaviors *IEEE/RSJ Int. Conf. on Intelligent Robots and Systems* (IEEE) pp 1656–62
- [47] Varin P and Kuindersma S 2018 A constrained Kalman filter for rigid body systems with frictional contact *Int. Workshop on the Algorithmic Foundations of Robotics*
- [48] Ljung L 1998 System identification *Signal Analysis and Prediction* (Berlin: Springer) pp 163–73
- [49] Van Overschee P and De Moor B 1994 N4sid: Subspace algorithms for the identification of combined deterministic-stochastic systems *Automatica* **30** 75–93
- [50] Arnold W F and Laub A J 1984 Generalized eigenproblem algorithms and software for algebraic Riccati equations *Proc. IEEE* **72** 1746–54
- [51] Goldberg B, Zufferey R, Doshi N, Helbling E F, Whittredge G, Kovac M and Wood R J 2018 Power and control autonomy for high-speed locomotion with an insect-scale legged robot *IEEE Robot. Autom. Lett.* **3** 987–93
- [52] Kwakernaak H and Sivan R 1972 *Linear Optimal Control Systems* vol 1 (New York: Wiley-Interscience)
- [53] Dai H and Tedrake R 2012 Optimizing robust limit cycles for legged locomotion on unknown terrain *IEEE 51st IEEE Conf. on Decision and Control* (IEEE) pp 1207–13
- [54] Manchester I R, Mettin U, Iida F and Tedrake R 2011 Stable dynamic walking over uneven terrain *Int. J. Robot. Res.* **30** 265–79
- [55] Cavagna G A, Heglund N C and Taylor C R 1977 Mechanical work in terrestrial locomotion: two basic mechanisms for minimizing energy expenditure *Am. J. Physiol.* **233** R243–61
- [56] Seyfarth A, Geyer H and Herr H 2003 Swing-leg retraction: a simple control model for stable running *J. Exp. Biol.* **206** 2547–55
- [57] Wisse M, Atkeson C G and Kloimwieder D K 2005 Swing leg retraction helps biped walking stability *5th IEEE-RAS Int. Conf. on Humanoid Robots* (IEEE) pp 295–300
- [58] Hobbelen D G and Wisse M 2008 Swing-leg retraction for limit cycle walkers improves disturbance rejection *IEEE Trans. Robot.* **24** 377–89
- [59] Vejdani H, Blum Y, Daley M and Hurst J 2013 Bio-inspired swing leg control for spring-mass robots running on ground with unexpected height disturbance *Bioinspir. Biomim.* **8** 046006
- [60] Pivovarov G and Byl K 2015 Reachability-based control for the active slip model *Int. J. Robot. Res.* **34** 270–87
- [61] Müller R, Birn-Jeffery A and Blum Y 2016 Human and avian running on uneven ground: a model-based comparison *J. R. Soc. Interface* **13** 20160529
- [62] Blum Y, Lipfert S W, Rummel J and Seyfarth A 2010 Swing leg control in human running *Bioinspir. Biomim.* **5** 026006
- [63] Daley M A 2018 Understanding the agility of running birds: sensorimotor and mechanical factors in avian bipedal locomotion *Integr. Comp. Biol.* **58** 884–93
- [64] Herr H M and McMahon T A 2001 A galloping horse model *Int. J. Robot. Res.* **20** 26–37
- [65] Karssen J D, Haberland M, Wisse M and Kim S 2011 The optimal swing-leg retraction rate for running *IEEE Int. Conf. on Robotics and Automation* (IEEE) pp 4000–6
- [66] Haberland M, Karssen J D, Kim S and Wisse M 2011 The effect of swing leg retraction on running energy efficiency *IEEE/RSJ Int. Conf. on Intelligent Robots and Systems* (IEEE) pp 3957–62
- [67] Karssen J D, Haberland M, Wisse M and Kim S 2015 The effects of swing-leg retraction on running performance: analysis, simulation, and experiment *Robotica* **33** 2137–55
- [68] Pearson K 1976 The control of walking *Sci. Am.* **235** 72–87
- [69] Pearson K G 2004 Generating the walking gait: role of sensory feedback *Progress in Brain Research* vol 143 (Amsterdam: Elsevier) pp 123–9
- [70] Ting L H and Macpherson J M 2005 A limited set of muscle synergies for force control during a postural task *J. Neurophysiol.* **93** 609–13
- [71] Chvatal S A and Ting L H 2013 Common muscle synergies for balance and walking *Frontiers Comput. Neurosci.* **7** 48
- [72] Hof A, Vermerris S and Gjaltema W 2010 Balance responses to lateral perturbations in human treadmill walking *J. Exp. Biol.* **213** 2655–64
- [73] Arellano C J and Kram R 2011 The effects of step width and arm swing on energetic cost and lateral balance during running *J. Biomech.* **44** 1291–5
- [74] Raibert M H 1986 *Legged Robots that Balance* (Cambridge, MA: MIT Press)
- [75] Raibert M, Chepponis M and Brown H 1986 Running on four legs as though they were one *IEEE J. Robot. Autom.* **2** 70–82
- [76] Srinivasan M and Holmes P 2008 How well can spring-mass-like telescoping leg models fit multi-pedal sagittal-plane locomotion data? *J. Theor. Biol.* **255** 1–7
- [77] Qiao M and Jindrich D L 2012 Task-level strategies for human sagittal-plane running maneuvers are consistent with robotic control policies *PLoS One* **7** e51888
- [78] Hodgins J K and Raibert M 1991 Adjusting step length for rough terrain locomotion *IEEE Trans. Robot. Autom.* **7** 289–98
- [79] Hodgins J K 1996 Three-dimensional human running *Proc. of IEEE Int. Conf. on Robotics and Automation* vol 4 (IEEE) pp 3271–6
- [80] Pratt J E 2000 Inherent robustness and natural dynamics in the control of bipedal walking robots, *PhD Thesis* Massachusetts Institute of Technology
- [81] Kim J-Y, Park I-W and Oh J-H 2007 Walking control algorithm of biped humanoid robot on uneven and inclined floor *J. Intell. Robot. Syst.* **48** 457–84

- [82] Gregorio P, Ahmadi M and Buehler M 1997 Design, control, and energetics of an electrically actuated legged robot *IEEE Trans. Syst. Man Cybern. B* **27** 626–34
- [83] Poulakakis I, Papadopoulos E and Buehler M 2006 On the stability of the passive dynamics of quadrupedal running with a bounding gait *Int. J. Robot. Res.* **25** 669–87
- [84] Koepl D, Kemper K and Hurst J 2010 Force control for spring-mass walking and running *IEEE/ASME Int. Conf. on Advanced Intelligent Mechatronics* (IEEE) pp 639–44
- [85] Koepl D and Hurst J 2014 Impulse control for planar spring-mass running *J. Intell. Robot. Syst.* **74** 589–603
- [86] Park H-W and Kim S 2015 Quadrupedal galloping control for a wide range of speed via vertical impulse scaling *Bioinspir. Biomim.* **10** 025003
- [87] Blickhan R and Full R 1993 Similarity in multilegged locomotion: bouncing like a monopode *J. Comput. Physiol. A* **173** 509–17
- [88] Kram R and Taylor C R 1990 Energetics of running: a new perspective *Nature* **346** 265
- [89] McMahon T A and Cheng G C 1990 The mechanics of running: how does stiffness couple with speed? *J. Biomech.* **23** 65–78
- [90] Blickhan R 1989 The spring-mass model for running and hopping *J. Biomech.* **22** 1217–27
- [91] Holmes P, Full R J, Koditschek D and Guckenheimer J 2006 The dynamics of legged locomotion: models, analyses, and challenges *SIAM Rev.* **48** 207–304
- [92] Seyfarth A, Geyer H, Günther M and Blickhan R 2002 A movement criterion for running *J. Biomech.* **35** 649–55
- [93] Heglund N C, Taylor C R and McMahon T A 1974 Scaling stride frequency and gait to animal size: mice to horses *Science* **186** 1112–3
- [94] Farley C T, Glasheen J and McMahon T A 1993 Running springs: speed and animal size *J. Exp. Biol.* **185** 71–86
- [95] Farley C T and Gonzalez O 1996 Leg stiffness and stride frequency in human running *J. Biomech.* **29** 181–6
- [96] Weyand P G, Bundle M W, McGowan C P, Grabowski A, Brown M B, Kram R and Herr H 2009 The fastest runner on artificial legs: different limbs, similar function? *J. Appl. Physiol.* **107** 903–11
- [97] Ferris D P, Louie M and Farley C T 1998 Running in the real world: adjusting leg stiffness for different surfaces *Proc. R. Soc. B* **265** 989–94
- [98] Schmitt J, Garcia M, Razo R, Holmes P and Full R J 2002 Dynamics and stability of legged locomotion in the horizontal plane: a test case using insects *Biol. Cybern.* **86** 343–53
- [99] Taylor C R, Schmidt-Nielsen K and Raab J L 1970 Scaling of energetic cost of running to body size in mammals *Am. J. Physiol.* **219** 1104–7
- [100] Snyder K L and Farley C T 2011 Energetically optimal stride frequency in running: the effects of incline and decline *J. Exp. Biol.* **214** 2089–95
- [101] Kim S and Park S 2011 Leg stiffness increases with speed to modulate gait frequency and propulsion energy *J. Biomech.* **44** 1253–8
- [102] Hamner S R and Delp S L 2013 Muscle contributions to fore-aft and vertical body mass center accelerations over a range of running speeds *J. Biomech.* **46** 780–7
- [103] Hasaneini S J, Macnab C J, Bertram J E and Leung H 2013 Optimal relative timing of stance push-off and swing leg retraction *IEEE/RSJ Int. Conf. on Intelligent Robots and Systems* (IEEE) pp 3616–23
- [104] Alexander R M 2003 *Principles of Animal Locomotion* (Princeton, NJ: Princeton University Press)
- [105] Ozcan O, Baisch A T, Ithier D and Wood R J 2014 Powertrain selection for a biologically-inspired miniature quadruped robot *IEEE Int. Conf. on Robotics and Automation* (IEEE) pp 2398–405
- [106] Doshi N, Jayaram K, Goldberg B and Wood R J 2017 Phase control for a legged microrobot operating at resonance *IEEE Int. Conf. on Robotics and Automation* pp 5969–75
- [107] Hildebrand M 1965 Symmetrical gaits of horses *Science* **150** 701–8
- [108] Jen E 2005 *A Repertoire of Biological, Ecological, and Engineering Case Studies* (Oxford: Oxford University Press)
- [109] Doshi N, Jayaram K, Goldberg B, Manchester Z, Wood R J and Kuindersma S 2018 Contact-implicit optimization of locomotion trajectories for a quadrupedal microrobot *Robot. Sci. Syst.* (<https://doi.org/10.15607/RSS.2018.XIV.041>)
- [110] Chen Y, Doshi N, Goldberg B, Wang H and Wood R J 2018 Controllable water surface to underwater transition through electrowetting in a hybrid terrestrial-aquatic microrobot *Nat. Commun.* **9** 2495
- [111] de Rivaz S, Goldberg B, Doshi N, Jayaram K, Zhou J and Wood R J 2018 Inverted and vertical climbing of a quadrupedal microrobot using electroadhesion *Sci. Robot.* **3**
- [112] Cruse H, Dürr V, Schilling M and Schmitz J 2009 Principles of insect locomotion *Spatial Temporal Patterns for Action-Oriented Perception in Roving Robots* (Berlin: Springer) pp 43–96